RSC Advances

High coercivity α-Fe2O3 nanoparticles prepared by continuous spray pyrolysis

SCHOLARONE™
Manuscripts

High coercivity α-Fe$_2$O$_3$ nanoparticles prepared by continuous spray pyrolysis

Rich Kant,[#1] Dinesh Kumar,[#1] and Viresh Dutta[1]

Photovoltaic Laboratory, Centre for Energy Studies, Indian Institute of Technology Delhi,

New Delhi-110016, India

Abstract

Surfactant free growth of α-Fe$_2$O$_3$ nanoparticles by continuous spray pyrolysis (CoSP) resulted in high coercivity (H_C). X-ray diffraction (XRD), Raman spectroscopy, and Fourier transform infrared spectroscopy (FT-IR) confirmed the formation of pure α-phase of Fe$_2$O$_3$. Scanning electron microscopy (SEM) showed a dimpled-morphology in samples grown at ≥800°C. XRD, SEM, Transmission electron microscopy (TEM) and temperature dependent magnetization data provided the evidence of presence of sub-structure in the α-Fe$_2$O$_3$ particles. The Morin transition in the sample grown at 1000°C is observed at 245 K with high coercivity (H_C) ~6 kOe at 300 K, which is among the highest reported in the literature. At 10 K, H_C ~10 kOe was observed for α-Fe$_2$O$_3$ grown at 600°C which is also the highest coercivity reported in literature. This remarkably high H_C observed at low temperature is correlated with the enhanced role of surface spins due to the surfactant free growth technique employed in the present work.

Keywords: High coercivity, Morin transition, Dimpled morphology, and Surface effects.

[1]Centre for Energy Studies, Indian Institute of Technology Delhi, New Delhi 110016. India.
 E-mail: dinesh1.goyal@gmail.com,   richucre@gmail.com;   Tel.   +9111-2659-6417;
fax. +9111-2659-1261.

[#]Equally contributing authors

I Introduction

Metal oxides have drawn great attention in recent years due to their distinctive electronic, chemical, optical, and thermal and magnetic properties.[1-9] Among various metal oxides synthesized, Fe_2O_3 nanomaterials have been of great interest because of broad applications in the areas of adsorbents, catalysis, pigments, ferrofluids, magnetic sensors and magnetic storage media.[10-14] Fe_2O_3 exists in four different crystalline polymorphs, namely, α-Fe_2O_3, β-Fe_2O_3, γ-Fe_2O_3 and ε-Fe_2O_3. α-Fe_2O_3 is thermodynamically the most stable polymorph of iron oxide with additional advantages such as non-toxicity, biocompatibility, corrosion resistance, and eco-friendliness.[15-16] α-Fe_2O_3 can be crystallized in the rhombohedral or hexagonal system with the space groups $R\bar{3}c$ or D_{3d}^6 respectively.[7] There are reports on the growth of α-Fe_2O_3 nanoparticles by various techniques such as solvothermal, hydrothermal, mechanochemical, sol gel, coprecipitation-annealing, thermal decomposition, surfactant mediation and microwave plasma.[14,17-20] All the techniques utilize surfactants for controlling the particle size, which affect the magnetic properties. We have employed a novel surfactant free Fe_2O_3 nanoparticle growth technique based upon continuous spray pyrolysis (CoSP). This growth method has several advantages over the conventional methods such as consuming less time for fabricating large amount of nanoparticles economically, requiring no additional post-fabrication treatment such as annealing and avoiding use of any surfactant/solvents for size control, though giving a large distribution of particle sizes due to atomized droplet size in the range of 10-100 μm for pneumatic type atomizer.[21-24] Absence of surfactant can lead to improved magnetic properties as is indeed observed and yield a high coercivity nanomaterial.

Materials with high coercivity (H_C) have applications in large memory devices,[25] permanent magnets[16] etc. Although there are some studies reporting a high value of coercivity in

2

α-Fe$_2$O$_3$,[26-29] yet reasons behind observed high coercivity is under debate[30] due to lack of understanding of the correlation between morphology, microstructure, inter-particle interactions, and magnetic properties of α-Fe$_2$O$_3$.[27] Highest coercivity value in case of α -Fe$_2$O$_3$ nanomaterials reported so far is ~6.2 kOe at 300 K[25] and 6 kOe at 4 K.[9]

In this work, high coercivity α-Fe$_2$O$_3$ particles fabricated using CoSP technique are reported, with the highest H_C ~10KOe at 10 K well above the value reported so far in literature and reasonably high H_C ~6 kOe at 300 K. The observed H_C values are interpreted in terms of substructure inside the particles, surface morphology and enhanced surface effects due to solvent/surfactant free growth employed in the present work.

II   Experimental details

Preparation of material

The continuous spray pyrolysis reactor was employed for the fabrication of α-Fe$_2$O$_3$ micro/nanoparticles into which the precursor solution (0.15M aqueous solution of Fe (NO$_3$)$_3$.9H$_2$O) was sprayed.[21] The three zones were kept at different temperatures, with the temperatures of 1st and 3rd zone (T$_1$ and T$_3$) kept constant at 350°C and 500°C respectively and the temperature of 2nd zone (T$_2$) varied from 400-1000°C. N$_2$ was used as carrier gas at a flow rate of 1.5 Kgf/cm^2.The precursor solution was sprayed at a constant flow rate of 2ml/min. The nanoparticles produced in the reactor were collected in a DI water bubbler connected at the outer end of the furnace. Samples prepared at different temperatures, T$_2$= 400, 600, 800 and 1000 °C are named as S400, S600, S800, and S1000, respectively.

Characterization

The structural data on all the samples was collected using X-ray diffractrometer (Rigaku ULTIMA-IV), with CuKα incident beam (λ= 1.54Å) over a 2Θ range of 30° to 80°. Raman Spectroscopy (Horiba Lab RAM HR Evolution) equipped with Ag ion 514nm laser at 20mW power was used for identification of phase of as prepared iron oxide samples. Fourier transform infrared (FT-IR) spectra were recorded by NICOLET iS50 FT-IR (ATR) spectrometer in the range of 400-4000 cm^{-1}. Morphology and Energy dispersive X-ray (EDX) analysis of the as synthesized particles was investigated by (ZEISS EVO-50 model) scanning electron microscope (SEM). The transmission electron microscopy (TEM) studies were made using JEOL-JEM-2100F electron microscope. Magnetization isotherms were measured in Quantum Design (PPMS Ever Cool-II) SQUID magnetometer in a magnetic field (H) up to 70 kOe. Magnetization (M) vs. temperature (T) measurements were performed in 10-300 K range following the zero field cooling (ZFC) and field cooling (FC) protocols in presence of constant field of 1kOe.

III   Results and discussion

Structural characterization

Fig. 1 shows the XRD pattern of as synthesized powder samples. Absence of diffraction peaks in the XRD pattern of S400 indicates the amorphous nature of this sample. But the high intensity peaks observed in the diffraction spectra of S600, S800 and S1000 confirm the crystalline nature of these samples. Full width at half maximum (FWHM) decreases with the increase of growth temperature (from 400 to 1000°C) which shows that the particle crystallinity is increased. All the observed peaks in the XRD pattern can be indexed to the rhombohedral structure of α-Fe$_2$O$_3$ with R$\bar{3}$C space group.[31] No peak corresponding to the other phases of the iron oxide is observed,

4

confirming the presence of only pure α-Fe$_2$O$_3$. Lattice parameters calculated from (104) and (110) diffraction peaks, a=b=5.02Å and c=13.69 Å, are in good concordance with JCPDS NO. 89-8104. The mean crystallite size of S600, S800 and S1000 samples are estimated from Debye-Scherrer formula[32] using FWHM of (104), (110), and (113) peaks and are found to be 19.8, 46.3 and 76.5 nm, respectively. The increased particle size can be caused by nanoparticles agglomeration with increasing temperatures.

Raman Spectroscopy

Raman Spectra (Fig. 2) confirm the presence of pure α-phase of Fe$_2$O$_3$ supporting the XRD data. The peaks at 222 and 495 cm^{-1} corresponds to A1g and the peaks at 244, 290, 406, and 608 cm^{-1} corresponds to E$_g$ vibrational modes of α-Fe$_2$O$_3$.[14] Unlike other techniques absence of any additional peak confirms the pure α-Fe$_2$O$_3$ phase fabrication by CoSP technique.

Fourier transform infrared (FT-IR) Spectroscopy

The chemical compositions of the S400-S1000 samples were examined by FT-IR spectroscopy shown in Fig. 3. Two prominent vibration bands can be seen in the region 400-600 cm^{-1} of FT-IR spectra. Band appearing at ~425 cm^{-1} and ~540 cm^{-1} can be attributed to bending vibration of O-Fe-O and stretching vibration of the Fe-O respectively.[6,33] The absence of any additional significant absorption peak in the spectrum again confirms the formation of pure α-Fe$_2$O$_3$ in all the samples.

Scanning electron microscopy and elemental analysis

Scanning electron microscopy (SEM) images for S400-S1000 are shown in Fig. 4. One can see the presence of broad distribution of particle sizes, in range of 0.2 to 2μm independent from growth temperature. The spherical shaped particles with smooth surface are observed for S400.

Fig. 4(b) shows that for S600 most of the particles are spherical, but the surface smoothness starts to decrease. In case of S800 pits on the surface in the form of dimples can be clearly seen. On further increasing the growth temperature to 1000^oC, compared to S800 the dimples on the surface of S1000 sample get deeper. So, one can say that increasing growth temperature is responsible for the morphology change (spherical to dimpled) observed in our samples.

The elemental composition of the S400-S1000 was further confirmed by the EDX measurements, shown in Fig. 5 (a-d), which shows that the primary components are Fe and O. As sample preparation involved the coating of carbon, so the presence of carbon-peak appeared at low energy. The absence of any other impurity peak indicates that the prepared samples are of high purity, in good agreement with XRD, Raman, and FT-IR results.

Transmission electron microscopy (TEM) studies

Transmission electron microscopy (TEM) was used to study the crystallinity, internal morphology, microstructure, and particle size present in the samples. The bright field TEM images of S400-S1000 samples are shown in Figs. 6(a1) to (d1), respectively. It can be seen that the particles present in S400 sample are spherical in shape. The presence of small irregularity starts to appear in S600 sample and with the increase in growth temperature the irregular shape becomes more prominent and can be seen in the form of dimples for S800 and S1000 samples. This observation is in consonance with the evolution of spherical to dimpled morphology observed in SEM. One can be seen that for S1000 sample particles are composed of nanoparticles subunits, but as we move from S800 to S400 sample the substructure starts to disappear. In order to understand this micro-structural behavior high magnification TEM images are recorded and are shown in Figs. 6(a2) to (d2) for S400 to S1000 samples, respectively. The

presence of nearly spherical sub-particles can be seen in all the samples. It can be seen that sub-particles are densely packed in S400 sample and with the increase of growth temperature the density starts to decrease. So, we can say that S400 sample consists of densely packed sub-particles and in case S600 sample the decrease in sub-particles density results in the porous nature and this becomes more prominent for S800-S1000 samples. Particle size distribution obtained from magnified TEM is shown in Figs. 6(a3) to (d3) for S400 to S1000 samples, respectively. The particle size distribution is found to be nicely fitted to log-normal distribution function. The mean particle sizes are determined to be 13.2 nm, 16 nm, 32.2 nm and 63.6 nm for S400, S600, S800 and S1000, respectively and found to be increasing with the increase in growth temperature as expected. Selected area diffraction (SAED) patterns of the samples S400-S1000 are also shown in Figs. 6 (a4)-(d4) for S400 to S1000 samples, respectively. Absence of any rings in SAED pattern of S400 confirms the amorphous nature of sample, thus supports the XRD data. The increase in ring pattern with the appearance of bright spots can be seen in S600 sample and these bright spots increases for S800 and S1000 samples confirming a further increase in crystalline nature as also observed in XRD.

Magnetic Measurements

Magnetization measurements were performed to see the effect of observed morphology and microstructure on the magnetic properties. Fig. 7 shows the isofield temperature (T) dependence of the magnetization (M) for all the samples, recorded in *ZFC* and *FC* protocols in the presence of 1 kOe magnetic field. The S400 and S600 samples do not exhibit the Morin transition, a sharp change in magnetization value between 300 - 10 K, usually observed in bulk hematite samples.[34,35] The non-observance of Morin transition in S400 and S600 samples can be correlated with the particle size as determined from TEM, as it is reported[7] to be suppressed in

samples having size smaller than 20 nm. The *ZFC-FC* curves of these samples display all the features typical of superparamagnetic particle systems, including a strong *FC-ZFC* irreversibility between the two curves (with low temperature M_{FC} value far above the maximum magnetization in the M_{ZFC} curve) and a Curie-Weiss (i.e., $1/T$ dependence of magnetization) like decay of the magnetization in the reversible region.[11,36-40] The blocking temperature (T_B), as inferred from the peak in *ZFC* is found to be 80 K and 110 K for S400 and S600 respectively. We can see that broadness of the *ZFC* peak increases with the increase of growth temperature from 400°C to 600°C and indicates the increase in particle size distribution.[37,38] It can be seen that for S800, *FC* and *ZFC* curves split significantly with blocking temperature increased to 140 K and broadness of *ZFC* curve increased compared to that for S600. Increase in broadness and split reflects the further increase in distribution of the particle sizes. Moreover, the *FC-ZFC* curves of S800 also reveal a Morin transition at T_M (Morin transition temperature) = 230 K, determined from differential of *ZFC* curve (shown as inset in Fig. 7c). For S1000 sample *FC* and *ZFC* curves overlap in the entire studied temperature range. The characteristic behavior of α-Fe_2O_3 i. e. Morin transition with T_M = 245 K, is determined from the sharp differential curve (inset in Fig. 7d). T_M values observed for S1000 is higher than for S800. It is reported that T_M and T_B increases with the increase in particle size.[35] So, we can conclude that size of particles increases monotonically with the increase of growth temperature from 400 °C to 1000 °C and this observed trend is in concordance with increase crystallite size (XRD) and particle size (TEM).

Fig.8 shows the *M-H* data recorded at 300 K and 10 K for the samples S400 to S1000, measured upto the highest available magnetic field of 70 kOe. The values of magnetization at highest applied magnetic field of 70 kOe (M_{70kOe}), remanent magnetization (M_r), and coercivity (H_C) are presented in Table I. It can be seen that *M-H* curves at 300 K for all the samples do not

reach to the saturation even at a maximum applied field. *M-H* curves of S400 and S600 exhibits a very small hysteresis loop with small values of M_r and H_C (Table I).

Table I: The values of H_C, M_r, and M_{70kOe} inferred from *M-H* at 300 K and 10 K.

Sample Name	300 K			10 K		
	M_{70kOe} (emu/g)	M_r (emu/g)	H_C (Oe)	M_{70kOe} (emu/g)	M_r (emu/g)	H_C (Oe)
S400	5.8	0.005	27	10.4	1.848	6295
S600	5.3	0.009	50	6.8	1.642	9840
S800	4.8	0.334	890	5.9	0.852	5001
S1000	4.4	0.452	6005	4.1	0.075	833

This kind of magnetic behavior is indicative of superparamagnetic nature of particles[41] and also supported by the observed *FC-ZFC* behavior. For S800, M_r increases to 0.334 indicates the ferromagnetic nature of sample and is generally observed above T_M in samples showing the Morin transition.[15] The central part of *M-H* loop has a kink with a H_C~890 Oe. The kink in the *M-H* curve, indicative of two types of particle sizes, is in consonance with simultaneous presence of blocking and Morin transition for this particular sample. On further increase of growth temperature to 1000°C (S1000), quite surprisingly, a high coercivity value of H_C ~6 kOe with M_r = 0.452 is observed. It may be pointed that, this H_C value is among the highest coercivity reported for α-Fe_2O_3 nanoparticles.[25] The magnetic behavior of α-Fe_2O_3 particles are generally affected by the microstructure and crystallite/particle sizes. Now the observed H_C values in S400-S1000 samples can be correlated with the increase in particle/crystallite size observed in *TEM*/XRD measurements. It is reported that α-Fe_2O_3 particles with size smaller than 20 nm show superparamagnetic behavior with zero M_r and H_C.[30,35] In our case, very small M_r and H_C values are observed for S400 and S600 with mean particle size < 20 nm. Small value of observed H_C in

this case is correlated with the interactions present between the particles as the magnetic measurements are performed by palletizing the powder samples and magnetic interactions are expected to be more prominent in powder samples than diluted and dispersed systems. High value of H_C ~0.9 kOe is observed for S800, where Morin transition is observed in addition to blocking temperature and it increases to ~6 kOe for S1000 where only Morin transition is observed. As the presence of sub-particle structure is clearly observed in TEM (Fig. 6) and this kind of substructure has been reported[8,15] to be the possible origin of observed large coercivity in α-Fe_2O_3 particles showing Morin transition. Other possible reason of high coercivity could be the presence of dimpled-morphology of the particles present in S800 sample. The increase of growth temperature to 1000°C results in increase in the depth of the dimples observed in S1000 (Fig. 4) and hence the coercivity is also increased. So, it can be concluded that the substructure present in the particles and the difference in morphology play the critical role in determining the large variation in the magnetic behavior and high coercivity.

Fig. 8 also shows the *M-H* data recorded at 10 K. M_{70kOe}, M_r and H_C values are given in Table I. For all the samples the *M-H* data is not saturating at all. It can be seen that M_{70kOe} increases at 10 K compared to that observed at 300K, for all the samples except S1000. The decrease in M_{70kOe} in S1000 is a signature of antiferromagnetic material[15] and is expected to be observed below T_M. The remarkably high values of H_C ~6.3, 10, 5 kOe are observed in S400, S600, and S800, respectively (Table I). H_C ~10 kOe observed at 10 K in S600 is the highest value reported so far in literature. In case of S1000, H_C~0.8 kOe below T_M and a small unclosed hysteresis loop is observed even at 70 kOe. These observed features points toward the presence of uncompensated spins present at surface of the particles.[7] The increase in coercivity with decrease in growth temperature can be understood in terms of enhancement of uncompensated

spins with decrease in particle size observed in *TEM*. With the decrease of particle size, an increase in the surface to volume ratio results in the increase in surface contributions and surface effects are reported to be enhanced at low temperature.[31] Therefore, the large increase in coercivity at 10 K with decreasing growth temperature is due to the decrease in particle size. But the remarkably high coercivity observed in our case, can be understood in terms of simplistic growth conditions and avoidance of any surfactants. The presence of surfactants on magnetic nanopartices makes the surface atoms magnetically inactive and spins of the atoms are not able to response at low temperature. Decrease in H_C to ~6.3 kOe in case of S400 compared to S600, even though the particle size is decreased, can be associated to the amorphous nature of the former .[6] So, the observed high coercivity is correlated with the increase of surface effects due to the decrease in the particle size and surfactant free growth employed in the present work.

IV   Conclusions

We have established that continuous spray pyrolysis can be used as a simple and convenient route to prepare the high coercivity α-Fe_2O_3 nanoparticles, with aqueous solution of Fe $(NO_3)_3$.$9H_2O$ as a precursor. XRD, Raman, EDX and FT-IR studies confirmed the pure phase of α-Fe_2O_3. SEM showed transition from spherical to dimpled morphology at temperature ≥ 800 ^oC. T_B and T_M are found to be growth temperature dependent and indicate increase in the particle size. TEM study clearly evidenced the presence of nearly spherical sub-structure in the form of nanoparticles in all the samples. At 300 K, coercivity (H_C) is found to in range of ~0.03- 6 kOe. The high H_C ~6 kOe in S1000 is ascribed to the sub-particle structure and dimpled morphology. The highest H_C ~ 10 kOe observed at 10 K for the sample prepared at 600 ^oC is related to increased fraction of magnetically active spins present on the surface on account of a surfactant free growth.

References

1   H. C. Zeng, *J. Mater. Chem.*, 2006, **16**, 649

2   C. Burda, X. Chen, R. Narayanan and M. A. El-Sayed, *Chem. Rev.*, 2005, **105**, 1025.

3   W. U. Huynn, J. J. Dittmer and A. P. Alivisatos, *Science,* 2002, **295**, 2425.

4   H. Mattoussi, L. H. Radzilowski, B. O. Dabbousi, E. L. Thomas, M. G. Bawendi and M. F. Rubner, *J.   Appl. Phys.*, 1998, **83**, 7965.

5   T. S. Ahmadi, Z. L. Wang, T. C. Green, A. Henglein and M. A. Elsayed, *Science,* 1996, **272**, 1924.

6   S.Mitra, S.Das, K.Mandal, and S.Chaudhuri, *Nanotechnology*, 2007, **18**, 275608.

7   J. Jacob and M. A. Khadar, *J. Magn. Magn. Mater.*, 2010, **322**, 614.

8   R. Yao and C. Cao, *RSC Adv.*, 2012, **2**, 1979.

9   V. Malik, S. Sen, D. R. Gelting, M. G.-Josifovska, M. Schmidt and P. Guptasarma, *Mater. Res. Express*, 2014, **1**, 026114.

10   C. Cannas, G. Concas, D. Gatteschi, A. Falqui, A. Musinu, G. Piccaluga, C. Sangregorio   and G. Spano, *Phys. Chem.Chem. Phys.*, 2001, **3**, 832.

11   N. Pailhe, A. Wattiaux, M. Gaudon and A. Demourgues, *J. Solid State Chem.*, 2008, **181**, 2697.

12   T. Ninjbadgar, S. Yamamoto and T. Fukuda, *Solid State Sci.*, 2004, **6**, 879.

13   R. Zboril, M. Mashlan and D. Petridis, *Chem. Mater.*, 2002, **14**, 969.

14   K. Rout, M. Mohapatra, S. Layek, A. Dash, H. C. Verma and S. Anand, *New J. Chem.*, 2014, **38**, 3492.

15   M. I. Dar and S. A. Shivashankar, *RSC Adv.*, 2014, **4**, 4105.

16   M. Tadic, N. Citakovic, M. Panjan, B. Stanojevic, D. Markovic, D. Jovanovi, and V. Spasojevic, *J. Alloys and Compd.*, 2012, **543**, 118.

17   J. P. Wilcoxon and P. P. Provencio, *J. Phys. Chem. B*, 1999, **103**, 9809.

18   C. T. Seip and C. Connor, *Nanostruct. Mater.*, 1999, **12**, 183.

19   J. Van Wonterghem and S. Morup, *Phys. Rev. Lett.*, 1985, **55**, 410.

20   W. Q. Jiang, H. C. Yang, S. Y. Yang, H. E. Horng, J. C. Hung, Y. C. Chen and C. Y. Hong, *J. Magn. Magn. Mater.*, 2004, **283**, 210.

21   N. Kumar, V. K. Komarala, V. Dutta, *Chem. Eng. J.*, 2014, **236**, 66.

22   G. L. Messing, S. C. Zhang, and G.V. Jayanthi, *J. Am. Ceram. Soc.*, 1993, **76**, 2707.

23   K. Okuyama and I. W. Lenggoro, *Chem.Eng. Sci.*, 2003, **58**, 537.

24   B. Xia, I. W. Lenggoro, and K. Okuyama, *Adv. Mater.*, 2001, **13**, 1579.

25   Y. Yang, J. B. Yi, X. L. Huang, J. M. Xue, and J. Ding, *IEEE T. Magn.*, 2011, **47**, 3340.

26   M. Tadic, N. Citakovic, M. Panjan, Z. Stojanovic, D. Markovic and V. Spasojevic, *J. Alloys Compd.*, 2011, **509**, 7639.

27   B. Vallina, J.D. Rodriguez-Blanco, A.P. Brown, L.G. Benning and J.A. Blanco, *J. Nanopart. Res.*, 2014, **16**, 2322.

28   C. Rath, K.K. Sahu, S. D. Kulkarni, S. Anand, S.K. Date, R. P. Das and N.C. Mishra, *App. Phys. Lett.*, 1999, **75**, 4171.

29   P. G. Bercoff and H. R. Bertorello, *Appl. Phys. A*, 2010, **100**, 1019.

30   F. Bodkar, M.F.Hansen, C. B. Koch, K.Lefmann, and S.Morup, *Phys. Rev. B*, 2000, **61**, 6826.

31   R. N. Bhowmik and A. Saravanan, *J. Appl. Phys.*, 2010, **107**, 053916.

32   S. Bagheri, K. G. Chandrappa and B. A. H. Sharifah, *Res. J. Chem. Sci.*, 2013, **3**, 62.

33   P. CAMBIER, *Clay Minerals*, 1986, **21**, 191.

34   N. Amin and S. Arajs, *Phy. Rev. B*, 1987, **35**, 4810.

35   C. Wu, P. Yin, C. O. Yang and Y. Xie, *J. Phys. Chem.B*, 2006, **110**, 17806.

36   D. Kumar, S. Chaudhary, and D. K. Pandya, *J. Appl. Phys.*, 2012, **112**, 083924.

37   D. Kumar, S. Chaudhary, and D. K. Pandya, *J. Appl. Phys.* 2013, **114**, 023908.

38   D. Kumar, S. Chaudhary, and D. K. Pandya, *J. Magn. Magn. Mater.,* 2014, **370**, 127.

39   Y. S. Koo, B. K. Yun and J. H. Jung, *J. Magn.*, 2010, **15**, 21.

40   S. Giri, S. Samanta, S. Maji, S. Ganguli and A. Bhaumik, *J. Magn. Magn. Mater.*, 2005, **285**, 296.

41   L. Machala, R. Zboril and A. Gedanken, *J. Phys. Chem. B*, 2007, **111**, 4003.

Figure captions

Fig. 1: X-ray diffraction (XRD) pattern of α-Fe$_2$O$_3$ samples prepared at different temperatures (a) S400, (b) S600, (c) S800, and (d) S1000.

Fig. 2: Room temperature Raman spectra of α-Fe$_2$O$_3$ samples prepared at different temperatures (a) S400, (b) S600, (c) S800, and (d) S1000.

Fig. 3: Room temperature FT-IR spectra of α-Fe$_2$O$_3$ samples (a) S400, (b) S600, (c) S800, and (d) S1000.

Fig. 4: SEM images showing particle morphology of α-Fe$_2$O$_3$ samples for (a) S400, (b) S600, (c) S800, and (d) S1000. Insets are displaying corresponding micrographs at higher magnification.

Fig. 5: EDX spectra of α-Fe$_2$O$_3$ samples prepared at different temperatures, (a) S400, (b) S600, (c) S800, and (d) S1000.

Fig. 6: Bright field TEM, high magnification TEM, lognormal distribution and SAED patterns of S400 (a1-a4), S600 (b1-b4), S800 (c1-c4) and S1000 (d1-d4) samples.

Fig. 7: Temperature dependence of *ZFC* and *FC* magnetization for (a) S400, (b) S600, (c) S800, and (d) S1000. Insets are corresponding differential *ZFC* curves.

Fig. 8: *M-H* loops recorded at 10 K and 300 K for (a) S400, (b) S600, (c) S800, and (d) S1000. The insets show extended view near the low field regime highlighting the presence of hysteresis.
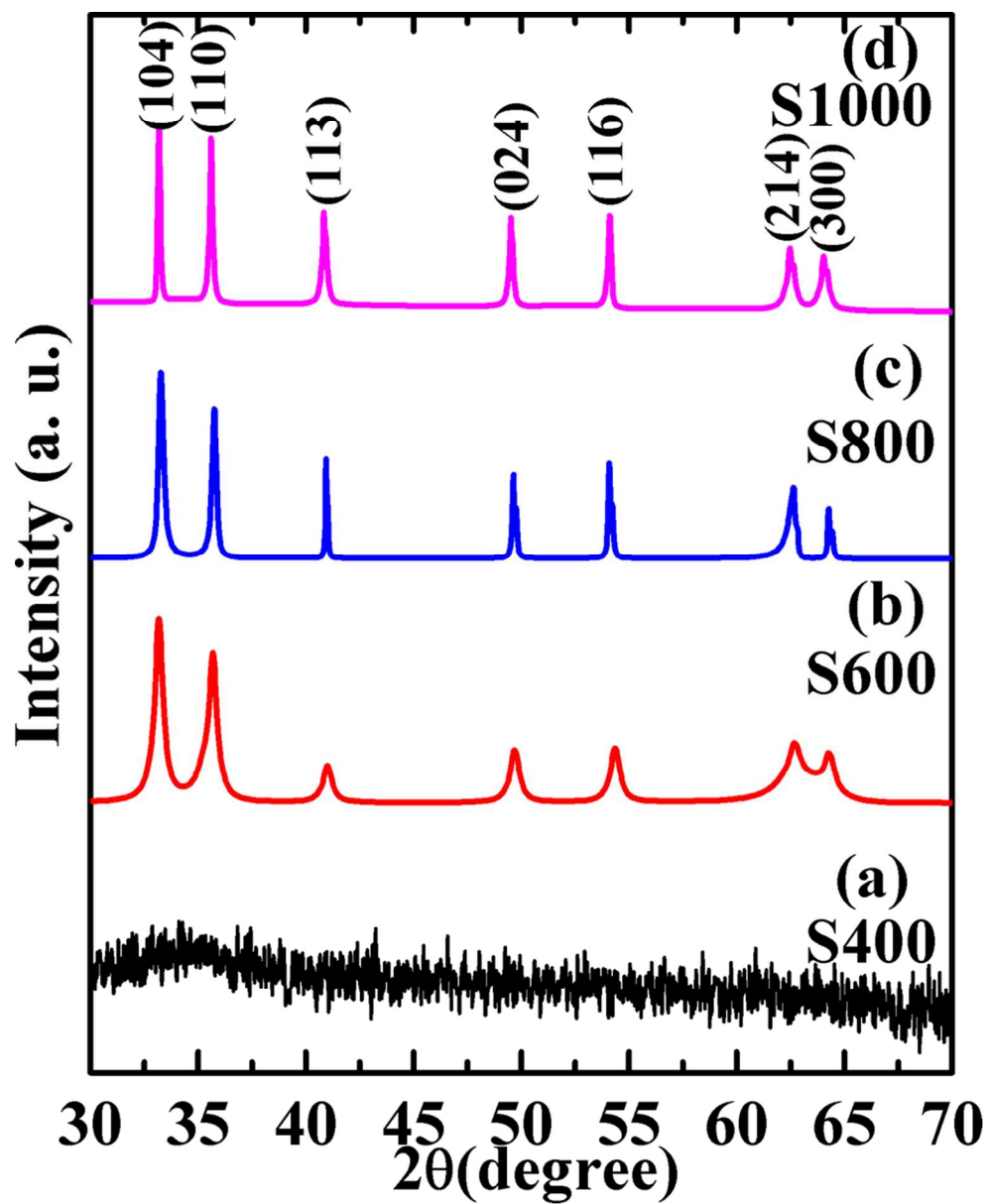
Fig. 1: X-ray diffraction (XRD) pattern of α-Fe2O3 samples prepared at different temperatures (a) S400, (b) S600, (c) S800, and (d) S1000.
85x104mm (300 x 300 DPI)
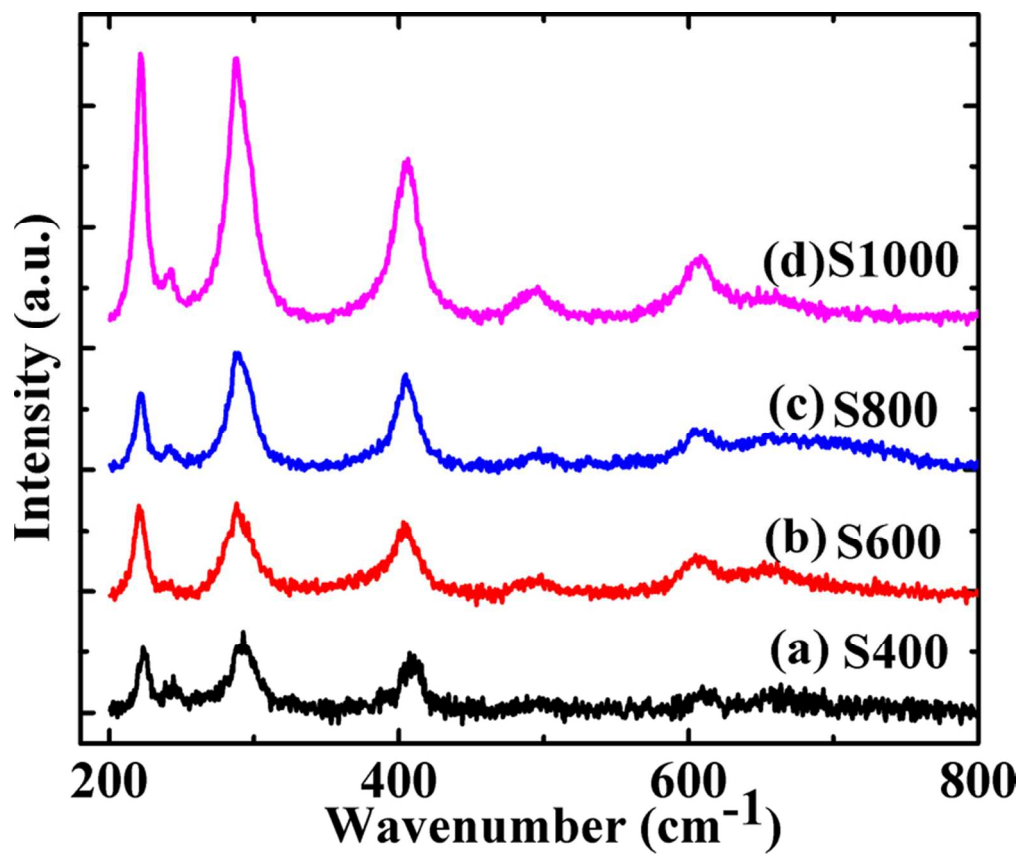
Fig. 2: Room temperature Raman spectra of α-Fe2O3 samples prepared at different temperatures (a) S400, (b) S600, (c) S800, and (d) S1000.
74x62mm (300 x 300 DPI)
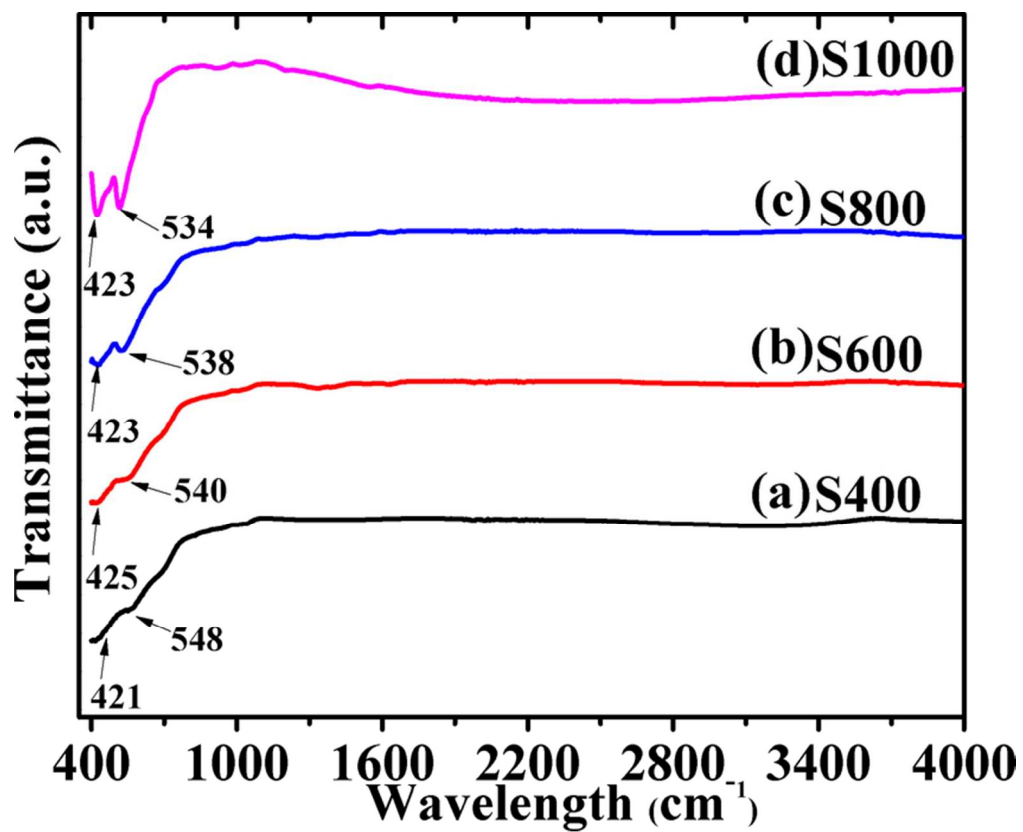
Fig. 3: Room temperature FT-IR spectra of α-Fe2O3 samples (a) S400, (b) S600, (c) S800, and (d) S1000.
71x58mm (300 x 300 DPI)
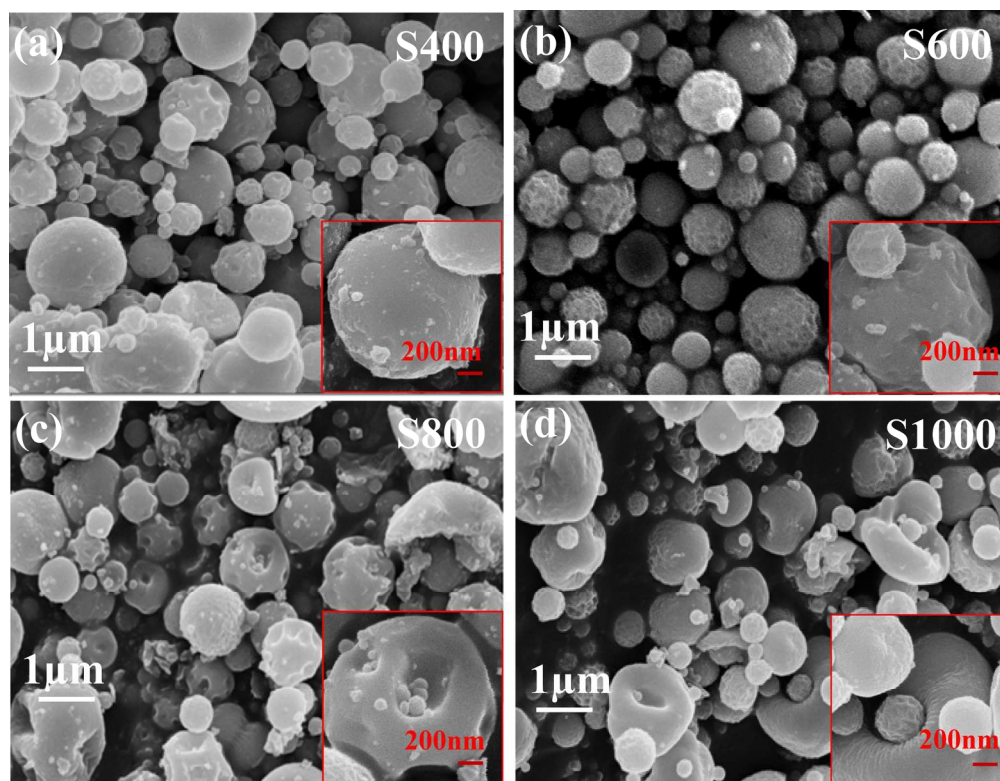
Fig. 4: SEM images showing particle morphology of α-Fe2O3 samples for (a) S400, (b) S600, (c) S800, and (d) S1000. Insets are displaying corresponding micrographs at higher magnification.
175x135mm (300 x 300 DPI)
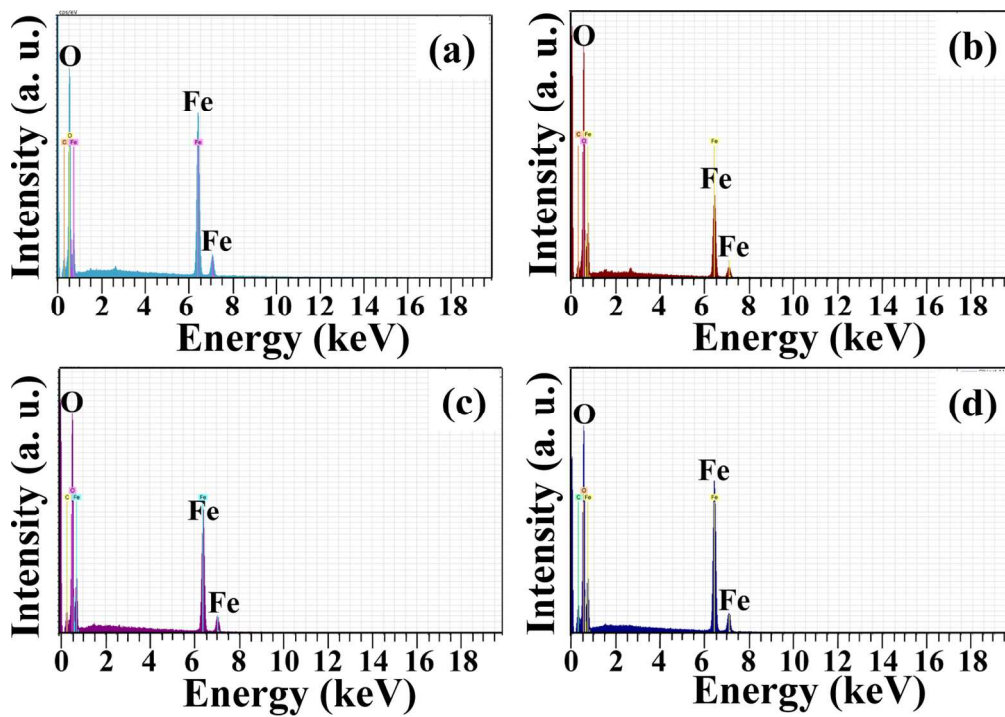
Fig. 5: EDX spectra of α-Fe2O3 samples prepared at different temperatures, (a) S400, (b) S600, (c) S800, and (d) S1000.
146x103mm (300 x 300 DPI)
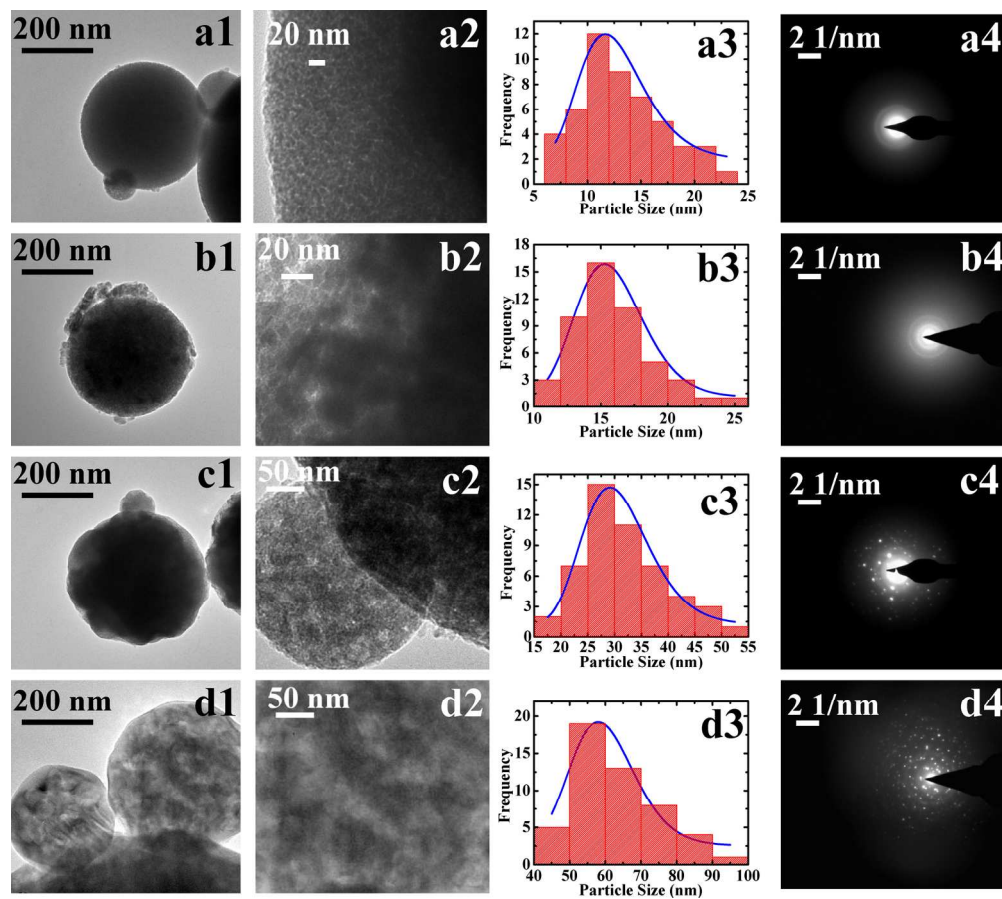
Fig. 6: Bright field TEM, high magnification TEM, lognormal distribution and SAED patterns of S400 (a1-a4), S600 (b1-b4), S800 (c1-c4) and S1000 (d1-d4) samples.
176x156mm (300 x 300 DPI)
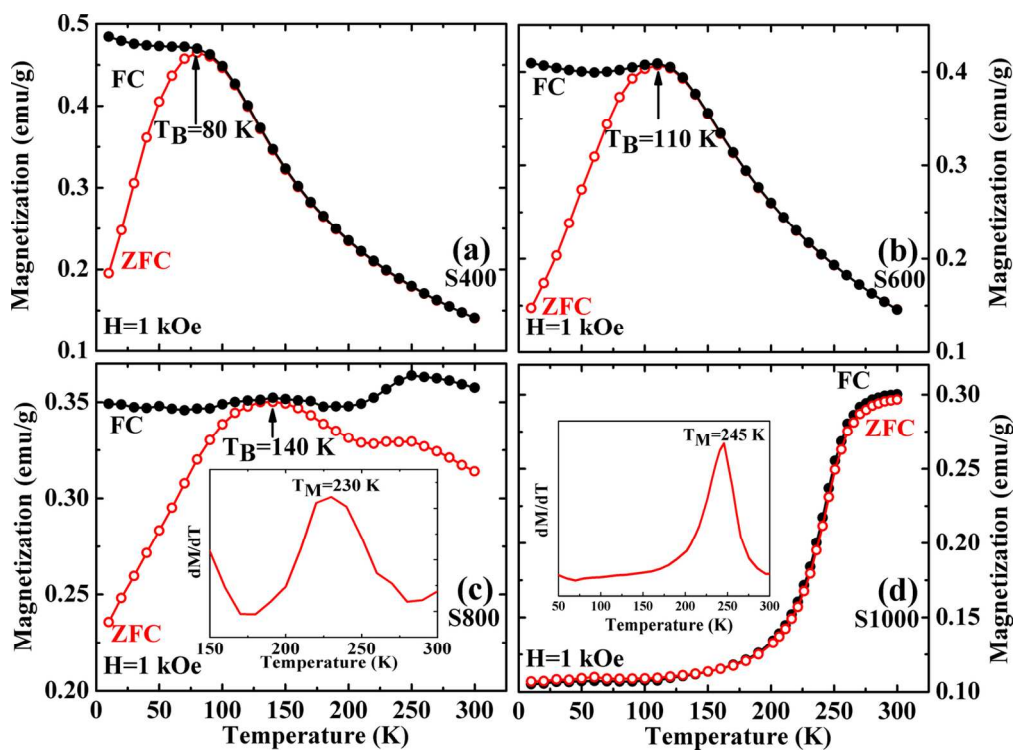
Fig. 7: Temperature dependence of ZFC and FC magnetization for (a) S400, (b) S600, (c) S800, and (d) S1000. Insets are corresponding differential ZFC curves.
132x97mm (300 x 300 DPI)
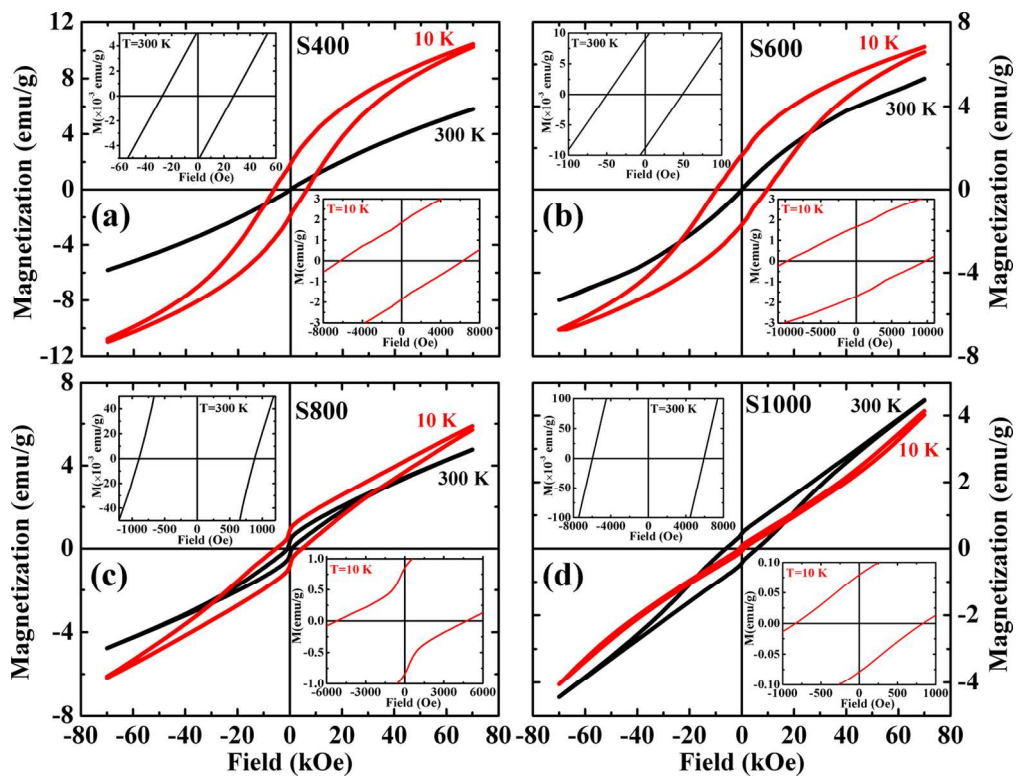
Fig. 8: M-H loops recorded at 10 K and 300 K for (a) S400, (b) S600, (c) S800, and (d) S1000. The insets show extended view near the low field regime highlighting the presence of hysteresis.
135x102mm (300 x 300 DPI)